

Design Optimization of Blood Shearing Instrument by Computational Fluid Dynamics

*Jingchun Wu, †James F. Antaki, ‡Trevor A. Snyder, ‡William R. Wagner,
‡Harvey S. Borovetz, and §Bradley E. Paden

**LaunchPoint Technologies, LLC, Goleta, CA; †Department of Biomedical Engineering & Computer Science, Carnegie Mellon University, Pittsburgh, PA; ‡Departments of Bioengineering and Surgery, University of Pittsburgh, and University of Pittsburgh McGowan Institute for Regenerative Medicine, Pittsburgh, PA; and §Department of Mechanical and Environmental Engineering, University of California, Santa Barbara, CA, U.S.A.*

Abstract: Rational design of blood-wetted devices requires a careful consideration of shear-induced trauma and activation of blood elements. Critical levels of shear exposure may be established in vitro through the use of devices specifically designed to prescribe both the magnitude and duration of shear exposure. However, it is exceptionally difficult to create a homogeneous shear-exposure history by conventional means. This study was undertaken to develop a Blood Shearing Instrument (BSI) with an optimized flow path which localized shear exposure within a rotating outer ring and a stationary conical spindle. By adjustment of the rotational speed and the gap dimension, the BSI is designed to generate shear stress magnitudes up to 1500 Pa for exposure time between 0.0015 and 0.20 s with a pressure drop of 100 mm Hg.

Computational fluid dynamics (CFD) revealed that a flow path designed by first-order analysis and intuition exhibited unfavorable pressure gradient, vortices, and undesirable regions of reverse flow. An optimized design was evolved utilizing a parameterized geometric model and automatic mesh generation to eliminate vortices and reversal flow and to avoid unfavorable pressure gradients. Analysis of the flow and shear fields for the extreme limits of the shear gap demonstrated an improvement in homogeneity due to shape optimization and the limitations of an annular shear device for achieving completely uniform shear exposure. **Key Words:** Hemolysis—Shear stress history—Left ventricular assist device—Computational fluid dynamics—Optimization.

Computational fluid dynamics (CFD) has proven to be a valuable tool for designing blood-wetted artificial organs (1–8). When integrated with parameterized models of the geometry, automatic mesh generation, and mathematical models of blood damage, CFD offers a faster means of optimization and is less reliant on empiricism than traditional trial-and-error approaches (3,8). With the advances in numerical methods, computer technology, and models of blood damage related to nonphysiologic flow conditions, CFD-based design has become a powerful tool for assessing the performance of the design and for reducing the number of prototypes and thus overall development cost. CFD-based design optimi-

zation has already been widely used in designing industrial pumps to increase hydraulic efficiency and improve other performance objectives such as cavitation (9). Effective application to blood pumps, however, requires additional quantitative models of blood trauma and shear-induced cellular activation. Although the precise mechanism of hemolysis still remains elusive, many studies have shown that it is correlated to the shear history to which blood is exposed. A general mathematical model of hemolysis is based on a power law of the form: $D = A\tau^\alpha t^\beta$, where D represents damage (often measured by the liberation of hemoglobin into the plasma), τ and t represent shear stress and exposure time, respectively, such as those introduced by Blackshear (10), Leverett (11), Hellums (12), Wurzinger (13), and Giersiepen (14), Yeleswarapu (15), and others. The model coefficients A , α , and β are empirically determined by regressing experimental data. These models have

Received May 2004; revised January 2005.

Address correspondence and reprint requests to Dr. Jingchun Wu, LaunchPoint Technologies LLC, 5735 Hollister Ave, Suite B, Goleta, CA 93117 U.S.A. E-mail: jwu@launchpnt.com

been proven useful in predicting and reducing hemolysis in blood-wetted devices. However, they suffer from two major limitations, both arising from the nonuniformity of shear stress and exposure history.

The first fundamental problem with the practical utilization of the power-law damage function is the extrapolation of the model to time-varying, nonhomogeneous shear history within a prototype device. The spatial nonuniformity may be addressed by implementation of a Lagrangian particle tracking method, wherein the damage function is applied theoretically to individual cells within the flow field. The temporal variation however, raises the question of how to map the damage criteria obtained by constant-shear experiments to a cyclical or arbitrary shear history found typically along the trajectory of a blood cell. A reasonable approach, introduced by Yeleswarapu et al. (15), is based on a theory of "damage accumulation." However it has yet to be thoroughly proven due to the difficulty in obtaining data from controlled experiments.

Regression of data for the power law function ideally requires an experiment wherein both the shear stress and exposure time are independently controllable. In addition, the flow conditions within the shear region of the experimental device must be reproducible. A variety of experimental devices has been used by others, including rotating cone-plates (16,17), and throttles through various nozzles (18,19). The cone-plate system has been attractive due to the relative homogeneity of the shear field. These devices, however, may generate secondary flow at high shear stress, and are not easily applicable to short-exposure experiments wherein initial transients may predominate. An innovative solution introduced by Heuser and Opitz (20) and recently described by Paul et al. (21), utilizes a Couette-type shear field in which shear stress level is controlled by the speed of a rotating cylinder and the exposure by the velocity of transverse flow across (through) the annulus. Unfortunately, the transverse flow is an annular Poiseuille velocity profile which is not uniform: zero at the boundary (due to nonslip condition) and maximal at the center of the annular gap. Consequently, the exposure history cannot be uniform.

A further confounding factor is the flow field near the entrance and exit of the shear space. The entrance flow may cause undesirable shear concentrations, which will confound the assumption of uniformity of shear. The flow exiting the annular gap may experience separation or recirculation, thereby prolonging exposure. Indeed the damage of blood

passing through the entrance and exit regions may overshadow the hemolysis within the defined "shear" region.

While the Couette-type experimental devices appear to be most desirable in decoupling the independent variables shear and time, this flow field within the "shear" region is known to be susceptible to Taylor instability (21). The resulting toroidal flow path would further disturb the uniformity of shear and exposure. This prompted Heuser et al. (20) to limit their experiments to shear stress less than 700 Pa, and recently Paul et al. (21) to 450 Pa, to avoid exceeding the critical Taylor number. It should be mentioned that previous CFD studies (22,23) attempting to apply the power law function proposed by Giersiepen (14) over-predicted hemolysis in simulated blood pumps.

This report presents the design optimization of a new Blood Shearing Instrument (BSI) by advanced CFD that aims to address some of the aforementioned limitations: (i) Taylor instability, (ii) limited shear stress range, and (iii) nonuniformity of shear and exposure.

MATERIALS AND METHODS

Design of the Blood Shearing Instrument (BSI)

The BSI depicted in Fig. 1 is intended to reproduce the range of shear stress–time exposure characteristics found in high-shear cardiovascular environments (e.g., rotary blood pumps, mechanical heart valves, hemodialysis catheters, occlusive arterial stenoses). It features a rotating ring that surrounds a stationary spindle, thereby creating an annular space through which blood is sheared. This configuration is chosen to avoid the possibility of Taylor instability, which may occur in conventional Couette-type viscometers with spinning inner rotors (20,21). Both rotor and spindle are slightly tapered to enable easy adjustment of the annular shear gap (from approximately 0.127–1.27 mm) via axial positioning of the spindle. The rotor, which is permanently mounted on ball-bearings, is actuated by a brushless-DC motor that is rotated between approximately 1000 and 10 000 rpm. The spindle itself is interchangeable, to allow experimentation with various materials, surface roughness, and chemical treatments. An additional feature of the BSI is a fluid-purged seal to prevent ingress of blood into the bearing area. This is maintained by constant, low-volume, flush of saline or other appropriate fluid by external positive displacement (roller) pump or pressure bag. This configuration avoids exposing blood to a mechanical seal. Such seals result in extremely high localized

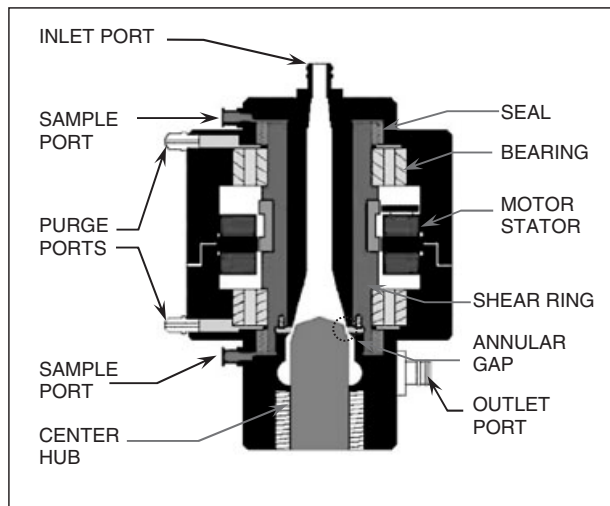


FIG. 1. Cross-sectional view of Blood Shearing Instrument (BSI). Blood enters port at top of assembly, and traverses through lumen, and exits through a radial outlet (bottom right). The center hub can be moved axially in relation to the stationary housing and the rotating "shear ring." The top and bottom faces of shear ring are purged with saline to obviate the need for a running mechanical seal. Sample ports are placed at the inlet and immediately below the shear ring to measure the effects of the high-shear exposure.

shear at the interface and generate local heating, both of which may introduce undesirable artifacts. The saline flush is typically prescribed to be several orders of magnitude less than the main blood flow (a few mL/min). Accordingly its influence on the shear rate was considered negligible.

The shear field within the annular gap is generated by a combination of two velocity gradients: one in the radial direction due to the rotation of the outer ring, and the other in the stream-wise direction caused by the pressure-driven flow through the ring. The net shear should be primarily dominated by the velocity gradient caused by rotation, which is principally uniform. The contribution of shear due to the pressure-driven flow should be minimized, since it causes a nonuniform shear which is maximal at the walls and theoretically zero at the centerline of the gap. Hence, in order to ensure a uniform concentration of shear stress within the gap, the ratio of the stream-wise Reynolds number, Re_x (see Eq. 1), to the circumferential Reynolds number, Re_U (see Eq. 2), should be kept as small as possible. Furthermore, to minimize the pressure drop, the length of the shear gap was designed to be relatively short (3.4 mm). Meanwhile, the entrance length of the blood lumen was designed to be long enough compared to the dimension of the gap to reduce the entrance and border effects. Nevertheless, the inevitably three-

dimensional flow field in this device may give rise to shear concentrations, secondary flows, and recirculation zones that may confound the requirement of uniformity and independence of shear and exposure. Therefore, a CFD-based optimization algorithm, which integrates a parameterized geometry model and automatic mesh generation, was applied to achieve the best compromise for the flow path.

CFD-based design optimization

CFD has been used for decades to simulate and analyze the fluid flow in many industries (24). By replacing physical experiments with numerical simulation, it becomes possible to automate the optimization process: by iteratively modifying a design until a specified performance index is maximized (minimized). When performed with a human expert in the loop, the process is usually referred to as CFD-based *design improvement* (9,25). When performed automatically, the designation of *design optimization* is applied. Both processes have been greatly facilitated recently by commercial CFD packages such as STAR-CD (CD-Adapco, New York, NY, U.S.A.) and CFX (ANSYS Inc., Canonsburg, PA, U.S.A.), which have integrated the advanced CFD solvers with constructive solid geometry modeling and automatic mesh generation.

In this study a novel CFD-based design optimization system was utilized incorporating both custom-written and commercial software. A commercial CFD code, STAR-CD, was chosen as the flow solver. It incorporates an element-based finite volume method suitable for unstructured and structured mesh with various turbulence models. It solves steady-state or transient flow with single or multiple, rotating or stationary frames of reference, including sliding mesh for turbomachinery and rotary blood pumps.

The flow geometry of the BSI was modeled parametrically based on B-spline curves and B-spline surfaces (26). An automatic mesh-generation code based on the elliptic method (27) was developed to generate the multiblock structured mesh with high-quality hexahedral cells to capture the complex flow field in the gap and volute. In order to accurately predict the reversal flow and eddies in BSI, particularly flow details within the gap, a highly refined mesh was used as shown in Fig. 2. A grid independency check was performed for all the cases to ensure a reasonable CPU time and appropriate density of mesh cells. It was found that about 300 000 cells across the gap region and in total about 1 000 000 cells for the whole computational domain were appropriate for the simulation.

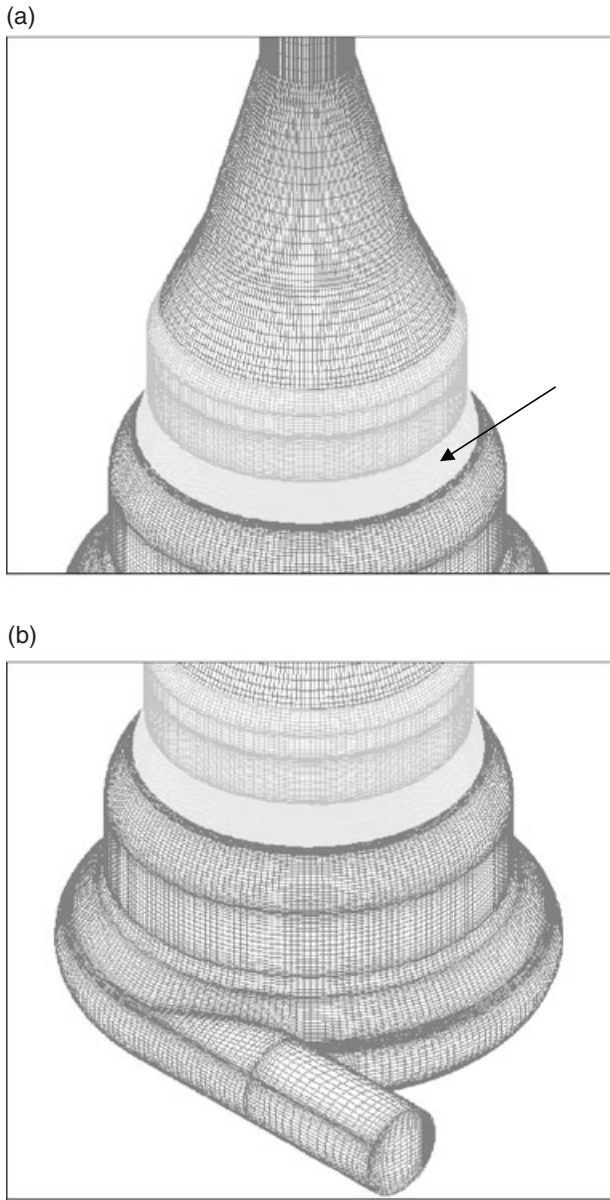


FIG. 2. Surface mesh of outer region of flowpath with about 1 000 000 cells. (a) Middle part including the rotational ring (arrow); (b) Bottom part including the volute.

Blood was modeled as a Newtonian fluid with a density of 1040 kg/m³ and a viscosity of 0.0035 Pa-s for these studies, which was justified based on the shear range under consideration (28). The Reynolds numbers in circumferential and stream-wise directions within the gap are defined, respectively, by:

$$Re_U = \frac{\rho \Omega R_i \delta}{\mu} \quad (1)$$

$$Re_S = \frac{\rho V_S \delta}{\mu} \quad (2)$$

Here, the subscript *U* represents the circumferential direction, and *S* indicates the stream-wise direction. Extensive CFD studies were performed for the BSI considering various gap dimensions δ from a nominal value of 0.127 to 1.27 mm, flow rates between 0.1 and 1.0 L/min, and the rotational speed ranging from 1000 to 10 000 rpm. For all the low flow (0.1 L/min) cases studied, the CFD studies showed quite uniform flow fields and localized shear stress distribution within the gap without separation and vortices upstream and downstream of the gap. This was observed for all combinations of gap dimensions δ and rotational speed studied. However, for the high-flow cases (1.0 L/min), separation and vortices were found just downstream of the gap for the initial design. This was especially true for the highest rotational speeds studied (10 000 rpm)

Two representative extreme cases, in which there is quite serious separation and recirculation downstream of the gap for the initial design, are presented here to demonstrate the effect of shape optimization upon the elimination of these undesirable flow features. The independent design parameters for these two cases are detailed in Table 1.

For Case 1, a laminar flow condition was assumed based on both Reynolds numbers of Re_S and Re_U . For Case 2, although Re_S is low, the Re_U is relatively high. Therefore, a low-Reynolds κ - ϵ turbulence model was used in this study. At the inlet of the flow domain a uniform axial flow velocity was imposed. At the outlet, zero stream-wise gradients were imposed for all variables. A second-order Linear Upwind Differencing (LUD) scheme (29) was employed in this study to assure accurate numerical solutions within the gap.

The shear stress in blood is comprised of viscous shear stress and Reynolds stress components, and its tensor is described by the following equation:

$$\tau_{ij} = \mu \left(\frac{\partial u_i}{\partial x_j} + \frac{\partial u_j}{\partial x_i} \right) - \overline{\rho u'_i u'_j} \quad (3)$$

Where μ is the fluid dynamic viscosity, and the last term on the right-hand side of Eq. 3 is the Reynolds stress tensor given by:

$$-\overline{\rho u'_i u'_j} = \mu_t \left(\frac{\partial u_i}{\partial x_j} + \frac{\partial u_j}{\partial x_i} \right) - \frac{2}{3} \rho k \delta_{ij} \quad (4)$$

TABLE 1. Main parameters for two computational cases

	Gap (mm)	Flow rate (L/min)	rpm	Re_U	Re_S
Case 1	0.127	1.0	10 000	557.6	71
Case 2	1.270	1.0	10 000	5576	71

Where μ_t is the turbulent viscosity, and δ is the Kronecker delta. For laminar flow the Reynolds stress tensor is zero.

For simplicity, a scalar stress as proposed by Bludszweit (30) can be obtained by the equation:

$$\tau = \left[\frac{1}{6} \sum (\tau_{ii} - \tau_{jj})^2 + \sum \tau_{ij}^2 \right]^{\frac{1}{2}} \quad (5)$$

Because blood contains about 45% red blood cells and about 55% plasma, strictly speaking, blood should be simulated by CFD based on transient Lagrangian (or Eulerian) multiphase flow models, where the plasma is taken as the continuous phase, while the red blood cells are taken as the dispersed phase. The motion of both phases interacts strongly via interphase momentum, mass, and heat transfer effects. In this way, the shear stress acting on red blood cells and the loading history can be accurately solved. However, due to the numerical difficulties in solving the multiphase flows and prohibitive CPU time involved, very few practical applications of multiphase flow models to CFD simulation of blood flows can be found. A reasonably accepted alternative is the use of a Lagrangian particle-tracking approach by postprocessing. A number of virtual particles are released from the inlet of the computational domain, which allows the shear stress history through the domain to be computed. Because the flow is almost axially symmetrical within the gap, only 30 particles along a radial direction at the inlet of the domain were released for each case.

RESULTS AND DISCUSSION

The initial flow geometry was defined based on first-order analysis and intuitive design. The basic parameters: gap size, length, and rotational speed were determined from closed-form solutions. The upstream and downstream contours were prescribed to achieve a smooth streamlined flow path devoid of sharp corners or crevices. This initial design was simulated and subsequently revised approximately five times to achieve a final “optimized” design. The flow simulations for each of the iterations were analyzed according to the objectives referenced above, particularly pressure drop, shear concentration, and flow stagnation. Improvements were made based on intuitive perturbations of the geometry, using the parametric geometric model, to minimize shear concentrations, pressure drop, and regions of stagnation.

The pressure contour plots for the region of primary interest, the annular gap between spindle and ring, are shown in Fig. 3. The original geometry is

shown in Fig. 3a,c, and the optimized geometry is shown in Fig. 3b,d. For Case 1 (small gap), because the stream-wise velocity magnitude is comparable to the circumferential velocity along the wall, the computed pressure drop is relatively high (about 22 400 Pa for the initial design) through the gap. For the initial design in Case 1, due to the relatively sudden expansion of the area downstream of the gap, the blood flow was observed to form a small unfavorable stream-wise pressure gradient downstream of the gap (see Fig. 3a). The optimized design alleviates the downstream kinetic energy concentration by smoothing the area downstream of the gap. The resulting pressure distribution as shown in Fig. 3b is more uniform, and does not display such an unfavorable pressure gradient as in Fig. 3a.

The pressure adjacent to the rotational ring is approximately proportional to $\Omega^2 r^2$ due to the effects of centrifugal force. Therefore, the isobaric surfaces are canted to the normal direction when the gap becomes wider, as displayed in Fig. 3c,d. For the original design with an acute conical angle, an unfavorable streamwise pressure gradient within and downstream the gap is exhibited (see Fig. 3c). The optimized design with a large conical angle, presents no such unfavorable streamwise pressure gradient (see Fig. 3d).

Figure 4a–d show the flow velocity patterns within a r - z plane near the gap for both designs. For both initial and optimized designs in Case 1, the stream-wise velocity within the gap presents a quite uniform distribution (not shown). However, for the initial design, a distinct vortex downstream of the gap was observed—as illustrated in Fig. 4a. This is clearly a consequence of the downstream unfavorable pressure gradient as observed in Fig. 3a. For the optimized design in Case 1 (Fig. 4b), the modified geometry was found to produce a uniform pattern within and downstream of the gap without any vortices. For the original design with large gap, Case 2 (Fig. 4c), the unfavorable streamwise pressure gradient causes a stagnation zone to move upward into the gap on the spindle, where a large toroidal vortex is established. The optimized design however, does not display any such vortex. Although the velocity downstream of the gap along the spindle wall is somewhat retarded, there is a sufficient favorable streamwise pressure gradient to overcome drag forces, providing positive axial flow through the passage (see Fig. 4d).

The computed scalar shear stresses within the gap in Cases 1 and 2 for two designs are shown in Fig. 5, which illustrates that both designs present a quite high concentration of shear stress within the gap, as desired. For the very small gap of $\delta = 0.127$ mm (Case

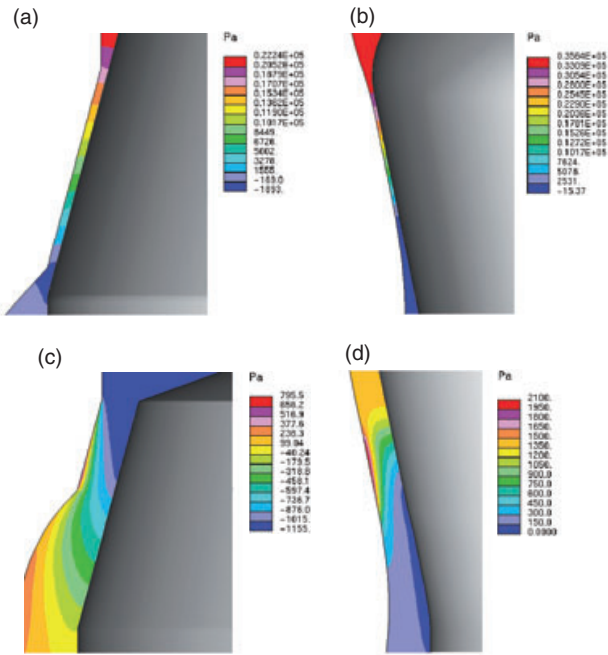


FIG. 3. Computed pressure contours within the gap through an r - z cut plane. (a) Initial design (Case 1); (b) Optimized design (Case 1); (c) Initial design (Case 2); and (d) Optimized design (Case 2).

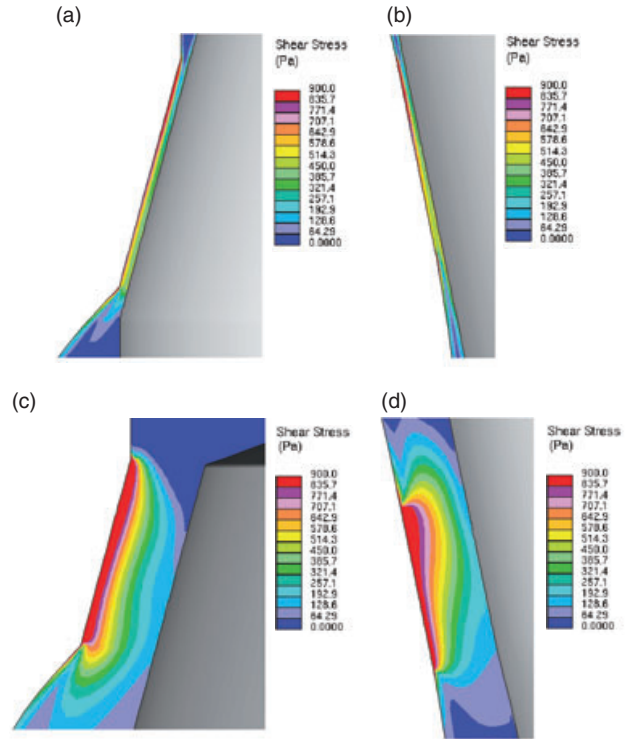


FIG. 5. Computed shear stress within the gap through an r - z cut plane.

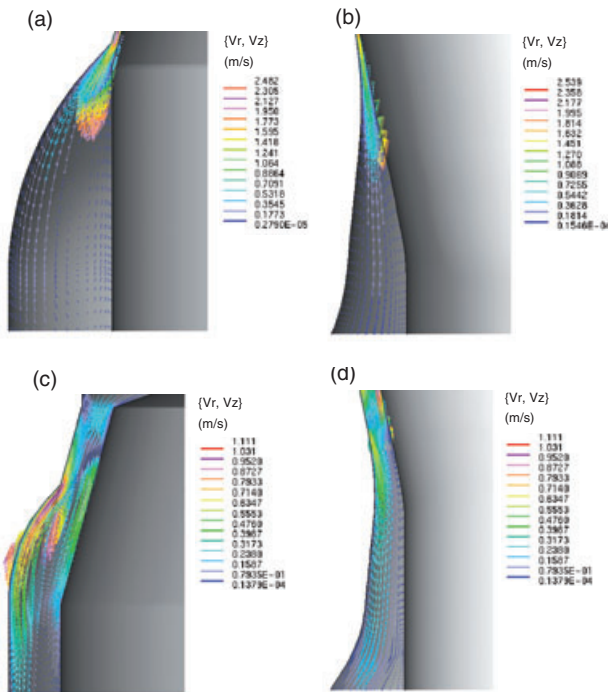


FIG. 4. Computed velocity vectors downstream of the gap through an r - z cut plane. (a) Initial design (Case 1); (b) Optimized design (Case 1); (c) Initial design (Case 2); and (d) Optimized design (Case 2).

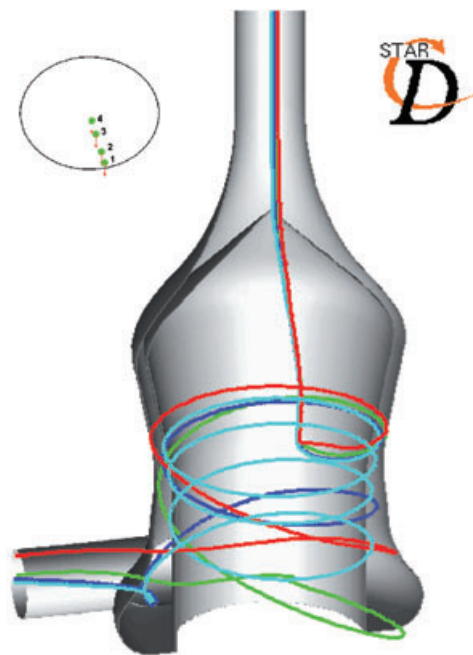


FIG. 6. Typical particle paths from inlet to outlet, indicating desired helical passage through the shear gap without recirculation upstream or downstream (Case 2, Optimized model).

1), the shear stress presents a quite uniform distribution, particularly toward the lower part of the gap. For the large gap of $\delta = 1.27$ mm (Case 2), because the rotational effects on the spindle are weaker, there is less homogeneity of shear across the gap (see Fig. 5c,d). Previous work (21) and our present studies showed that the concentration of shear stress within the gap depends heavily on the ratio of Re_s/Re_U and the absolute value of gap width, δ . Uniformity of the shear stress within the gap was more readily assured for small gap δ and small Reynolds ratio Re_s/Re_U . In spite of our best attempts, these CFD studies showed that the variation of conical angle of the spindle and the geometric profiles did not significantly improve the shear stress concentration within the gap, although it can eliminate the vortices and reversal flow.

The typical trajectories of four selected particles in BSI for optimized design with a gap of 1.27 mm are shown in Fig. 6. When particles enter the gap region, they are affected by the rotational ring and thereby flow helically downstream of the gap and finally enter the spiral volute before exiting. The particle history in Fig. 7 shows the change of shear stress with exposure time along the four selected particle trajectories. Figure 8 shows the change of shear stress along the pathline through the shear gap region. Particles are seen to experience high shear stress and short exposure time when they pass through the shear gap region. For particle 1 passing through the gap near the outer rotational ring, it experiences the highest shear stress. For particle 4, as it flows near the inner spindle, it experiences the lowest shear stress. For particles passing through a uniform shear stress field

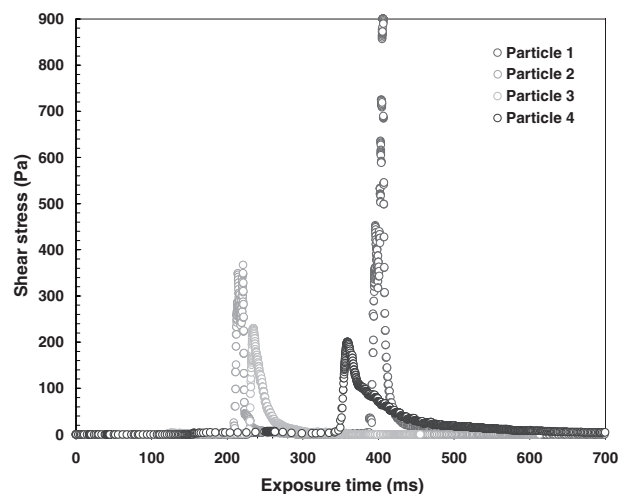


FIG. 7. Shear stress history for four particles for Case 2 (Optimized model).

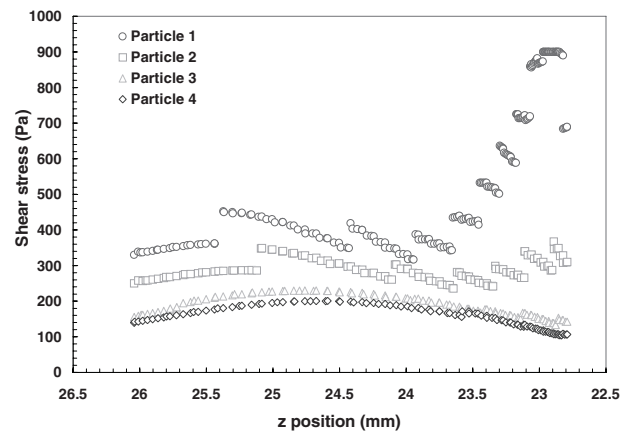


FIG. 8. Axial variation of shear stress through the shear gap for the four particles of Fig. 7.

at short time scales, the blood damage can be estimated by the direct use of the correlation of Gier siepen (14). However, if the shear stress field is nonuniform, the total damage incurred in a particle is assumed to be accumulated linearly within every very short time step, Δt_i as proposed by Bludszuweit (31) as in the following:

$$D_i = \sum_{i=\text{inlet}}^{\text{outlet}} 3.62 \times 10^{-7} \tau^{2.416} \Delta t^{0.785} \quad (6)$$

The mean blood damage estimated for 30 particles is listed in Table 2.

One of the objectives of this instrument will be to validate this and other models for adult and pediatric blood exposed to chronic mechanical support

CONCLUSIONS

A CFD-based optimization design approach, with the integration of the parameterized geometry model and automatic mesh generation, was described in this study. The method was successfully applied to the development of a specialized blood shearing instrument (BSI). Extensive CFD simulations have shown that the velocity, pressure, and shear fields are far more complex than would be anticipated from first-order approximation. Secondary flows, entrance effects, and the three-dimensionality of the flow field conspire to confound the achievement of both uniform shear stress and exposure time isolated to a confined shear gap.

TABLE 2. Computed mean blood damage D

Case 1 (Initial)	Case 1 (Optimized)	Case 2 (Initial)	Case 2 (Optimized)
0.0096	0.0091	0.0608	0.0543

Nevertheless, geometric improvements were achieved that alleviated some of the problems associated with the initial, intuitive design. The optimized model eliminates vortices downstream of the gap, and achieved satisfactory performance for a very wide range of gap widths, flow rates, and rotational speeds. This study has demonstrated that CFD-based optimization, incorporating a parameterized geometry model and automatic mesh generation, is a very useful and effective means to achieve a prescribed flow performance without time intensive trial and error.

The optimized geometry resulting from these analyses will be used to construct the Blood Shearing Instrument, BSI, described herein, for subsequent experimental studies of shear-induced trauma and activation of blood-formed elements. Detailed comparison between the numerically calculated and in vitro obtained hemolysis will be presented in a future report. The successful application of this technique encourages the future application to other blood-wetted devices.

Acknowledgment: This study was supported in part by NIH Contract HHSN2682-00448 129C (N01-HV-48192), "Pediatric Circulatory Support," to the University of Pittsburgh.

REFERENCES

- Okamoto E, Hashimoto T, Inoue T, Mitamura Y. Blood compatible design of a pulsatile blood pump using computational fluid dynamics and computer-aided design and manufacturing technology. *Artif Organs* 2003;27:61–7.
- Mitoh A, Yano T, Sekine K, et al. Computational fluid dynamic analysis of an intra-cardiac axial flow pump. *Artif Organs* 2003;27:34–40.
- Goto A, Nohmi M, Sakurai T, Sogawa Y. Hydrodynamic design system for pumps based on 3-D CAD, CFD, and inverse design method. *ASME J Fluids Eng* 2002;124:329–35.
- De Wachter D, Verdonck P. Numerical calculation of hemolysis levels in peripheral hemodialysis cannulas. *Artif Organs* 2002;26:576–82.
- Watanabe N, Karsak O, Neudel F, et al. Simulation of the BP-80 blood pump. *Artif Organs* 2001;25:733–9.
- Grigioni M, Daniele C, D'Avenio G, Barbaro V. The influence of the leaflets' curvature on the flow field in two bileaflet prosthetic heart valves. *J Biomech* 2001;34:613–21.
- Burgreen GW, Antaki JF, Wu ZJ, Holmes AJ. Computational fluid dynamics as a development tool for rotary blood pumps. *Artif Organs* 2001;25:336–40.
- Antaki JF, Ghattas O, Burgreen GW, He B. Computational flow optimization of rotary blood pump components. *Artif Organs* 1995;19:608–15.
- Lakshminarayana B. An assessment of computational fluid dynamic techniques in the analysis and design of turbomachinery? The 1990 Freeman Scholar Lecture. *ASME J Fluids Eng* 1991;113:315–52.
- Blackshear PL Jr, Dorman FD, Steinbach JH, Maybach EJ, Singh A, Collingham RE. Shear, wall interaction and hemolysis. *Trans Am Soc Artif Intern Organs* 1966;12:113–20.
- Leverett LB, Hellums JD, Alfrey CP, Lynch EC. Red blood cell damage by shear stress. *Biophys J* 1972;12:257–73.
- Hellums JD. 1993 Whitaker Lecture: Biorheology in thrombosis research. *Ann Biomed Eng* 1994;22:445–55.
- Wurzinger LJ, Blasberg P, Schmid-Schonbein H. Towards a concept of thrombosis in accelerated flow: rheology, fluid dynamics, and biochemistry. *Biorheology* 1985;22:437–50.
- Giersiepen M, Wurzinger LJ, Opitz R, Reul H. Estimation of shear stress-related blood damage in heart valve prostheses—in vitro comparison of 25 aortic valves. *Int J Artif Organs* 1990;13:300–6.
- Yeleswarapu KK, Antaki JF, Kameneva MV, Rajagopal KR. A mathematical model for shear-induced hemolysis. *Artif Organs* 1995;19:576–82.
- Pohl M, Wendt MO, Koch B, Vlastos GA. Mechanical degradation of polyacrylamide solutions as a model for flow induced blood damage in artificial organs. *Biorheology* 2000;37:313–24.
- Alkhamis TM, Beissinger RL, Chediak JR. Effect of hirudin on platelet deposition to an artificial surface during low-stress shear flow of whole blood. *Biomaterials* 1993;14:865–70.
- Forstrom R. *A New Measure of Erythrocyte Membrane Strength: The Jet Fragility Test*. Minneapolis, MN: University of Minnesota, 1969.
- Umezumi M, Yamada T, Fujimasu H, et al. Effects of surface roughness on mechanical hemolysis. *Artif Organs* 1996;20:575–8.
- Heuser G, Opitz R. A Couette viscometer for short time shearing of blood. *Biorheology* 1980;17:17–24.
- Paul R, Apel J, Klaus S, Schugner F, Schwindke P, Reul H. Shear stress related blood damage in laminar Couette flow. *Artif Organs* 2003;27:517–29.
- Yano T, Sekine K, Mitoh A, et al. An estimation method of hemolysis within an axial flow blood pump by computational fluid dynamics analysis. *Artif Organs* 2003;27:920–5.
- Song X, Throckmorton AL, Wood HG, Antaki JF, Olsen DB. Computational fluid dynamics prediction of blood damage in a centrifugal pump. *Artif Organs* 2003;27:938–41.
- Docter A, Min K. Stability of axial flow in an annulus with a rotating inner cylinder. *Phys Fluids A Fluid* 1992;4:2446–55.
- Burgreen GW, Antaki JF, Griffith BP. A design improvement strategy for axial blood pumps using computational fluid dynamics. *ASAIO J* 1996;42:M354–60.
- Rogers DF. *An Introduction to NURBS: With Historical Perspective*. San Francisco, CA: Morgan Kaufmann Publishers, 2001.
- Thompson JF, Warsi ZUA, Mastin CW. *Numerical Grid Generation: Foundations and Applications*. North-Holland, New York: Elsevier Science Pub. Co. distributor, 1985.
- Schmidt-Schonbein H, Wells R. Rheological properties of human erythrocytes and their influence upon the anomalous viscosity of blood. *Ergeb Physiol* 1971;63:124–219.
- Shyy W, Thakur S, Wright J. Second-order upwind and central difference schemes for recirculating flow computation. *AIAA J* 1992;30:923–32.
- Bludszuweit C. Three-dimensional numerical prediction of stress loading of blood particles in a centrifugal pump. *Artif Organs* 1995;19:590–6.
- Bludszuweit C. Model for a general mechanical blood damage prediction. *Artif Organs* 1995;19:583–9.